An ionicity rationale to design solid phase metal nitride reactants for solar ammonia production

Ronald Michalsky, Peter H. Pfromm

Published Version Information

Citation: Michalsky, R., & Pfromm, P. H. (2012). An ionicity rationale to design solid phase metal nitride reactants for solar ammonia production. Journal of Physical Chemistry C, 116(44), 23243-23251.

Digital Object Identifier (DOI): doi:10.1021/jp307382r

Publisher's Link: http://pubs.acs.org/doi/abs/10.1021/jp307382r

An ionicity rationale to design solid phase metal nitride reactants for solar ammonia production

Ronald Michalsky[1, 2, #], Peter H. Pfromm[2,*]

[1] NSF IGERT associate in biorefining, [2] Department of Chemical Engineering, 1005 Durland Hall, Kansas State University, Manhattan, Kansas, 66506, United States

Abstract

Ammonia is an important fertilizer component and could be used as a convenient hydrogen carrier. This work studies a solar thermochemical reaction cycle that separates the reductive N_2 cleavage from the hydrogenation of nitrogen ions to NH_3 without using electricity or fossil fuel. The hydrolysis of binary metal nitrides of magnesium, aluminum, calcium, chromium, manganese, zinc, or molybdenum at 0.1 MPa and 200-1000°C recovered up to 100 mol% of the lattice nitrogen with up to 69.9 mol% as NH_3 liberated at rates of up to 1.45×10^{-3} mol NH_3 (mol metal)$^{-1}$ s^{-1} for ionic nitrides. These rates and recoveries are encouraging when extrapolated to a full scale process. However, nitrides with lower ionicity are attractive due to simplified reduction conditions to recycle the oxidized reactant after NH_3 formation. For these materials diffusion in the solid limits the rate of NH_3 liberation. The nitride ionicity (9.96-68.83% relative to an ideal ionic solid) was found to correlate with the diffusion constants (6.56×10^{-14} to 4.05×10^{-7} cm^2 s^{-1}) suggesting that the reduction of H_2O over nitrides yielding NH_3 is governed by the activity of the lattice nitrogen or ion vacancies, respectively. The ionicity appears to be a useful rationale when developing an atomic-scale understanding of the solid-state reaction mechanism and when designing prospectively optimized ternary nitrides for producing NH_3 more sustainably and at mild conditions compared to the Haber Bosch process.

*) Corresponding Author: e-mail: pfromm@ksu.edu; phone: +1 785-532-4312; fax: +1 785-532-7372

[#]) Current address: Brown University, School of Engineering, Box D, 182 Hope Street, Providence, RI 02912, United States

Keywords: Solar radiation, Heterogeneous catalysis, Transition metal nitride, Transition metal oxide, Nitrogen diffusion, Mulliken population analysis

1. Introduction

Energy, water, and food have been cited by Nobel laureate R. Smalley in order of priority as the top three problems that mankind will face in the next decades[1]. Solar energy is essentially inexhaustible and environmentally benign. Employing solar energy to solve society's most demanding challenges, however, requires efficient harvesting of this relatively dilute, intermittent, and geographically non-homogeneous energy source[2].

Man-made ammonia (NH_3) has been recognized as to some extent responsible for the "green revolution" of the first half of the 20th century. In other words, it provides the basis of nutrition for a large portion of the human population on earth. Global production of NH_3 is currently about 130 million metric tons (t) annually[3]. Ammonia is produced industrially via heterogeneous catalysis that cleaves N_2 and hydrogenates nitrogen to NH_3 in a single step conducted at some of the most severe conditions in the chemical industry of up to 30 MPa and 500°C[4]. The compression work required for the technically sophisticated synthesis accounts for about 16% of the 28-37 GJ t^{-1} NH_3 consumed by the process[5]. Approximately 45% of the global H_2 production is absorbed as feedstock in the synthesis of NH_3[6]. The H_2 feedstock is generated on-site from fossil resources (mainly natural gas, coal or Naphtha), leading to significant fossil-based CO_2 emissions[4] and production of NH_3 in a few hundred large-scale centralized facilities world-wide[7]. Given the increasing global population and the potential of NH_3 as a "perfect hydrogen carrier"[8,9] and as a convenient alternative fuel in compression-ignition engines[10,11], direct synthesis of NH_3 from N_2, H_2O and sunlight may contribute to a sustainable solution to two of our most demanding challenges, energy and food.

Substantial research efforts have pursued the synthesis of NH_3 at ambient pressure[7]. NH_3 has been synthesized electrochemically or electrocatalytically[12-16], e.g., at the cathode of an electrochemical cell that is cleaving N_2[13] and H_2O to generate O^{2-} which is oxidized at the anode

to O_2[15]. Alternatively, homogeneous catalysis via N_2 reduction with transition metal complexes that give substantial yields of NH_3 when reacted with acid or H_2 has attempted to mimic the enzymatic catalysis of N_2 fixation in the liquid phase[17-20]. Albeit promising, both approaches have not yet reached maturity. Electrochemical synthesis relies on electricity and requires novel electrolyte and electrode materials to increase NH_3 formation rates[15]. A major obstacle of the biomimetic approach[18] is the external reducing equivalent (mostly a sacrificial alkali metal or pH adjustment) that is required for generating the dinitrogen complex from a high oxidation state halide complex[17-19].

This work pursues an alternative strategy that separates the N_2 cleavage from the nitrogen protonation (Scheme 1). Conceptually (with generalized stoichiometry), an oxidized inorganic material (M_cO_d) can be reduced with a suitable reducing agent (R) at elevated temperatures:

$$(1) \qquad \frac{a}{bc} M_c O_d + \frac{ad}{bc} R \leftrightarrow \frac{a}{b} M + \frac{ad}{bc} RO$$

with M being a metal and lower case letters indicating stoichiometric coefficients. The reaction accomplishes storage of the 2p electrons of oxygen in the metal. This can be achieved with concentrated solar radiation[2], that is, harvesting photons from the entire insolation spectrum as reducing equivalents[21-24]. Dependent on the free energy of formation of the metal, the remaining reducing equivalents required for the thermochemical charge transfer are supplied by a relatively weak reducing agent[18,25]. This may be H_2 or biomass with syngas as a beneficial co-product[26-28].

The generated reactant can thereafter provide the reducing power for the six-electron reductive cleavage of N_2 (forming N^{3-} ions in the solid state) and splitting of H_2O (yielding the metal oxide, the desired NH_3, and possibly H_2) without electricity or a fossil fuel:

$$(2) \qquad \frac{a}{b} M + \frac{1}{2} N_2 \leftrightarrow \frac{1}{b} M_a N_b$$

(3) $$\frac{1}{b}M_aN_b + \frac{ad}{bc}H_2O \leftrightarrow \frac{a}{bc}M_cO_d + NH_3 + \left(\frac{ad}{bc} - \frac{3}{2}\right)H_2$$

This separation of N_2 cleavage and protonation allows optimizing the equilibrium positions and kinetics of each reaction conducted at favorable temperatures and near 0.1 MPa.

Previous studies have outlined the likely economic competiveness of this concept[26,28,29]. Realization of the reaction cycle, however, requires research for a reactive material that balances conflicting thermochemical properties and technical requirements[28]. These are in particular: (i) acceptable yields and kinetics of the N_2 reduction and protonation of the lattice nitrogen near 0.1 MPa, (ii) reduction of the oxidized reactant (recycling) at temperatures that can be contained physically in an industrial-scale solar furnace (preferably below 1500°C), (iii) use of moderate quantities of a sustainable reducing agent, and (iv) significant energy conversion efficiencies (comparing raw materials plus solar energy with the energy contained in the NH_3 and perhaps syngas produced). The "degree of freedom" to control the reduction temperature and the quantities of reducing agent and byproducts by adjusting the reactant composition is illustrated with supporting material for this paper that is available online. Here the hydrolysis yield and kinetics, and the impact of this step on the overall process efficiency are the main subjects.

2. Thermochemical theory and reaction mechanism

2.1 Materials composition determining energy conversion efficiencies

Figure 1A maps the ratios of heat released during the N_2 reduction or NH_3 formation relative to the energy absorbed in the oxide reduction for various binary nitride/oxide pairs[28,30]. The calculation indicates high theoretical ratios of the heating value of the generated solar-based energy carrying molecules[31] (NH_3 and syngas) to the supplied solar and chemical energy of about 52 to 85%. This worst case assumes no in-process heat recovery, separate metal reduction and nitridation, and use of nitrides that are expected to yield ammonia.

Predominantly ionic nitrides (e.g., Mg_3N_2 or Ca_3N_2) liberate large quantities of heat during their hydrolysis (Fig.1A). This limits their attractiveness for the proposed concept since this energy can not be easily integrated at the higher temperatures required for the endothermic oxide reduction step. On the other hand, binary transition metal nitrides with relatively high NH_3 equilibrium yields (e.g., Mn_4N or Nb_2N, Fig.1B) will require large quantities of chemical reducing agent due to unfavorable stoichiometric compositions (e.g., 4 mol C per mol NH_3 for a Mn_4N/MnO reactive material relative to 3/2 mol C per mol NH_3 for a Mg_3N_2/MgO reactant). Although well-studied for their refractory properties[32,33] hydrolysis of nitrides and NH_3 formation kinetics have been rarely reported[27,34-36]. Pourbaix diagrams providing information on corrosion mechanisms are typically only available for pure elements[37]. Bonding in metal nitrides appears not well understood[38].

Determining an optimum reactant composition is a complex task of balancing contradictory requirements. Finding trends in the chemical reactivity and reaction kinetics is an essential first step in understanding material properties and in rational materials design[39]. Figure 2 shows that a higher number of d electrons correlates with reduced stability of the nitride due to the higher number of electrons in nonbonding orbitals weakening the metal-nitrogen bond[39]. Recognizing that this bond[38] has to be stable enough to reduce 0.1 MPa N_2 but weak enough[28] to avoid excessive liberation of heat during hydrolysis illustrates the importance of understanding the electronic structure[7,39,40] of the metal-nitrogen bond. This will be inevitable for the design of a novel, perhaps ternary[41], optimized reactant for the reactive NH_3 synthesis.

2.2 Possible reaction mechanism

In lieu of a complete quantitative description of the overall NH_3 formation mechanism, which exceeds the scope of this work, a schematic of the hypothetical reaction mechanism is given in Chart 1. The overall process converting N^{3-} ions and H_2O to O^{2-} and NH_3 is envisioned

as a succession of six steps: Water is (1) assumed to be adsorbed by a vacant surface site on the metal oxide and, thereafter, due to (2) diffusion of metal ions and electrons through the oxide, (3) reduced to H^+ and OH^-. This forms a metal hydroxide that may decompose to an oxide at elevated temperatures. The continuous growth of the oxide shell is enabled by (4) diffusion of nitrogen and oxygen through the oxide. The liberated nitrogen ion is (5) protonated to NH_3 and, depending on the Brønsted acidity of the metal ions[36], (6) desorbed from the oxide surface.

As a starting point, the present study evidences the diffusion of lattice nitrogen through the oxide and attempts to characterize its effect on the NH_3 formation kinetics. Section 4.1 and 4.2 characterize the kinetics of the NH_3 formation via hydrolysis of seven nitrides with different bonding properties. The efficiency of liberating the lattice nitrogen and protonating it to NH_3 is addressed in Section 4.3. Section 4.4 introduces the nitride ionicity as a rationale to screen for optimized reactants. Correlating the partial electric charge of the lattice nitrogen to the reaction characteristics of the bulk material will be shown to enable an atomic-scale understanding of the reaction mechanisms and activation barriers in the future.

3. Experimental

3.1 Metal nitridation

The nitrides of Ca, Mn and Mo were prepared (Fig.3)[38] from ca. 2 g of metal powder heated from 400°C to 700°C (Mn) or 750°C (Ca, Mo)[42] in a quartz boat inside of a tube furnace (60 mm ID, 1 m length, quartz, model HTF55347C, temperature controller model CC58434C, Lindberg/Blue). Mn and Mo were pre-treated at 60°C for 10 min to remove water. The heating rate r_H can be represented as $r_H = At + B$, where t is the heating time in min, A = -9.29°C min^{-2}, and B = 82.1°C min^{-1} ($R^2 > 0.90$). N_2 was always supplied at 0.1 MPa, i.e., 1.83 ± 0.02 $l_{(STP)}N_2$ min^{-1} (Ca, Mn), or diluted with H_2, i.e., 1.09 ± 0.01 $l_{(STP)}N_2$ min^{-1} mixed with 0.364 ± 0.003

$l_{(STP)}H_2$ min^{-1} (Mo). The nitridation temperature was held for 120 (Mn), 180 (Mo) or 240 min (Ca) respectively and cooling was at about -4.87°C s^{-1} at < 1 min, -50.6°C min^{-1} at 1 min to ≤ 10 min, and -3.63°C min^{-1} at > 10 min. The α-Ca_3N_2/Ca_2N product was milled with pestle and mortar. All Ca-containing chemicals were handled and stored under Ar. All solids were stored under Ar or N_2 at 4°C.

3.2 Metal nitride hydrolysis

To describe the reaction kinetics of the lattice nitrogen seven metal nitrides (Table 1) with varying bonding character were reacted at three different temperatures with steam (Fig.3). To remove residual O_2 the furnace was purged for ca. 10 min with 0.5-0.9 $l_{(STP)}N_2$ min^{-1} before each experiment. Nitride powder was placed into a quartz boat (0.5 g, except 1 g Cr_2N, i.e., 5.82 x 10^{-1} to 1.23 x 10^1 mmol total lattice nitrogen), introduced at 100°C into the furnace, and heated to 200-1000°C. Heating rates r_H can be approximated (R^2 = 0.75-0.83, see Section 3.1) with A = -6.85°C min^{-2} and B = 50.2°C min^{-1} (at 200-300°C), A = -4.23°C min^{-2} and B = 61.4°C min^{-1} (500-600°C), or A = -3.59°C min^{-2} and B = 82.8°C min^{-1} (1000°C) respectively. Final temperatures were held for 60 min and steam was supplied at 0.8 ± 0.1 $ml_{(STP)}H_2O$ min^{-1}.

The gas leaving the furnace was routed through a liquid absorbent (25 ± 5 $ml_{(STP)}$ ice-cold 10 mM HCl). To estimate the yield of absorbed NH_4^+, 5 ml samples were taken at 0, 1, 5, 10 and 60 ± 0.5 min (Mg_3N_2, AlN, Ca_3N_2, and Zn_3N_2) or 0 (this includes the heating phase), 5, 10, 30 and 60 ± 0.5 min (Cr_2N, Mn_4N, and Mo_2N) after the reaction temperature was reached. After 60 min the furnace was opened and cooled (at -0.90 to -8.7 °C s^{-1} at < 10 min, -8.8 to -82 °C min^{-1} at < 10 min, and -1.1 to -18°C min^{-1} at > 10 min) to below 100°C. All solids were stored under Ar (Mg_3N_2, Ca_3N_2) or air at 4°C. All liquids were stored at room temperature.

3.3 Solid state analysis

Powder X-ray diffraction (XRD, Miniflex II diffractometer, Cu-target X-ray tube, 30 kV / 15 mA output, diffracted beam monochromator, Rigaku) was used (5-80 °2θ range, 1 or 10 °2θ/min scan speed, 0.02 data points/°2θ, continuous mode) for quantitative solid phase identification (PDXL Software Version 1.6.0.0). To confirm metal nitridation energy-dispersive X-ray spectroscopy (EDS) was employed using scanning electron microscopy (SEM) (20 keV, S-3500N, Hitachi; Link Pentafet 7021 X-ray detector and Inca Energy X-ray analysis software, both Oxford Instruments). Nitride particles were imaged by SEM before and after reacting with steam at 500°C. All weights were determined using an AE260 DeltaRange balance (± 0.1 mg, Mettler). The specific BET surface area was analyzed by NanoScale Inc., Manhattan, KS.

3.4 Liquid and gas phase analysis

NH_3 absorbed by the liquid absorbent was analyzed in triplicate with an NH_3 Ion Selective Electrode and a pH/ISE Controller (model 270) (both Denver Instrument), combined with the liquid level in the absorption vessel (error ca. ± 5 ml). The uncertainty of NH_3 concentrations was estimated as the average of one standard deviation of about 65 liquid samples analyzed in triplicate. The outlet of the absorption vessel was equipped with an NH_3 gas detection tube (0.25-3 or 5-70 ppm NH_3 detection range, Dräger).

3.5 Chemicals

Solid chemicals were AlN (99.8% pure, -325 mesh), Mn metal (99.9% pure, -325 mesh), Zn_3N_2 (99.9% pure, -200 mesh), and Mo metal (99.95% pure, -325 mesh) all from Noah Technologies; Ca metal (99% pure, granular) and NH_4Cl (99.5%, extra pure) both from Acros Organics; Mg_3N_2 (99.6% pure, -325 mesh, AlfaAesar); Cr_2N (98% pure, -100 mesh, Prochem); and NaOH (99.6%, certified ACS pellets, Fisher Scientific). Glassware was cleaned with acetone (certified ACS, Fisher Scientific). All gases (H_2, N_2, and Ar) were UHP Zero grade (Linweld).

H_2O was deionized (Direct-Q 3 UV, Millipore) and degassed with Ar. HCl (12.1 N, certified ACS Plus) was from Fisher Scientific.

3.6 Nitride characterization

Table 1 shows the major bulk nitride phases identified via XRD. The BET specific surface area of the materials is consistent with the literature[27,34,35,42]. The surface area of the nitrides that have been prepared from their elements is of the same order of magnitude as for purchased Cr_2N and about one order of magnitude below the specific surface area of Mg_3N_2, AlN and Zn_3N_2. Whether this may affect NH_3 yields is addressed in Section 4.2. Values of the partial electronic charge of the lattice nitrogen[43-53], q_N, are summarized in Table 2.

3.7 Data processing

To determine the hydrolysis reaction kinetics, the yield of NH_3, X_{NH3}, is reported as molar ratio of NH_3 captured by the acidic absorbent (n in mol) at a given time, t, relative to the lattice nitrogen of the reactant before the reaction:

$$(4) \qquad X_{NH_3} = \frac{n_{absorbed\ NH_3,t}}{n_N} = \frac{\sum_{t=0-60\,\mathrm{min}} \left(c_{NH_3,t} - c^*_{NH_3}\right) V_t}{m_r \sum_{i=all\ nitrides} b_i x_i M_i^{-1}}$$

where c_{NH3} in mol L^{-1} is the concentration of NH_3 detected in the absorbent, the asterisk marks pure water used as a reference, V in L is the sample volume, m_r in g is the mass of metal nitride powder reacted, b is a stoichiometric coefficient (see Eq.3), x in g g^{-1} is the nitride weight fraction (Table 1), and M in g mol^{-1} is the molar mass. The initial reaction rate, r_0, is calculated analogously from a tangent to the data point collected at Δt = 5 min.

4. Results and Discussion

4.1 NH_3 liberation kinetics from p- and d-block nitrides

It is of utmost importance to determine limiting processes that impede a rapid and efficient conversion from nitride to ammonia. The rate-limiting process of a heterogeneous reaction may be mass transfer or chemical reaction, k_r, where k marks a specific rate constant. Mass transfer by diffusion occurs in the gas phase, described by k_g, or in the solid phase, k_s. To determine the rate-limiting step three shrinking-core models for spherical particles of unchanging size[54] were applied:

$$k_g t = X_{NH_3} \quad (5)$$

$$k_s t = 1 - 3 \times (1 - X_{NH_3})^{2/3} + 2 \times (1 - X_{NH_3}) \quad (6)$$

$$k_r t = 1 - (1 - X_{NH_3})^{1/3} \quad (7)$$

The specific rate constants fitted[23,34] in the time interval Δt_{fit} with a maximum R^2 are summarized in Table 3. Representative graphs of the NH_3 yield versus the reaction time (at the temperature that resulted in maximum X_{NH3}) are given in Figure 4. As an aside, the yield of NH_3 after 60 min is in most cases below the yield determined after 10 or 30 min respectively. This is presumably due to unwanted stripping of the absorbent by the steam routed from the reactor through the wash bottle after the reactor. Based on minimizing the residual sum of squares between the experimental data and the employed shrinking core models, a solid-state diffusion limitation (Eq.6) describes the formation of NH_3 from the tested p- and d-block nitrides (with few exceptions, see Table 3) best.

Solid-state diffusion limited NH_3 formation (Chart 1) is in agreement with the low yield of NH_3 via corrosion of chromium nitrides or stainless steel with dissolved nitrogen[27,33]. The NH_3 formation from Mn_4N, Zn_3N_2 and of β-Mo_2N[55] appears to follow a diffusion limited mechanism over a relative broad range of reaction temperatures and times. Hydrolysis of hot pressed AlN

particles has been found to yield only 0.3% Al_2O_3 after 30 hrs at 1000°C[32]. Also, a 2 mol% oxidation of fine AlN powder has been reported when hydrolyzing the nitride for 60 min at 900°C[34]. On the other hand, NH_3 from AlN and H_2O at below 100°C[35] and up to 70 mol% conversion via hydrolysis for 60 min at 1000°C have been reported as well[34]. This demonstrates the hydrolysis of the corrosion-resistant AlN depends significantly on the steam temperature (Table 3) and pressure, and the nitride particle size[32,34,35]. Liberation of NH_3 from AlN is represented well by a solid-state diffusion limited process (Table 3).

Supporting liberation of nitrogen from the bulk, projecting the nitride unit cells on the BET surface area of the bulk material allows an estimate of the maximum yield of a pure surface reaction (independent of the orientation of the crystal facets) with 0.07-0.80 mol% N from Mn_4N, CrN, Cr_2N, $Mn_6N_{2.58}$, Mo_2N, AlN or 2.34 mol% N from Zn_3N_2 respectively. Compared to the higher yields of lattice nitrogen found here (Fig.4) this supports the formation of NH_3 from the bulk of these materials involving the transport of lattice nitrogen from the bulk (approximately 13-490 nm below the particle surface) to the solid/gas interface.

In summary, diffusion limitations in the solid state appear to be the most plausible kinetic limitation for the NH_3 liberation via H_2O splitting over nitrides of Al, Cr, Mn, Zn, or Mo.

4.2 NH_3 liberation kinetics from s-block nitrides

A case will be made that hydrolysis of Mg_3N_2 or Ca_3N_2 respectively appears to follow a mechanism that is limited by gas phase diffusion (Eq.5) rather than solid-state diffusion. Opposed to the hydrolysis of Zn_3N_2 (Fig.4), diffusion limitation in the gas phase represents the liberation of NH_3 from Mg_3N_2 or Ca_3N_2 respectively best at all tested temperatures (Table 3).

The minimum initial reaction rates for these nitrides at 300°C may originate from the opposing effects of high reactant concentrations at low temperatures (about 25-16 mol H_2O m^{-3} at 200-500°C, assuming an ideal gas) and short residence times of the meta-stable NH_3 product at

high temperatures (about 13-8 s at 200-500°C). Furthermore, accounting for the difference in the average particle diameter, d_p, ($k_g \sim d_p^{-1}$)[54] between Mg_3N_2 and Ca_3N_2 particles (Table 1) yields a "corrected" specific rate constant k_g for Ca_3N_2 in the range of 0.47-1.72 times k_g for Mg_3N_2. Thus, the delayed NH_3 formation observed during the hydrolysis of Ca_3N_2 can be explained to a large part with the difference in specific surface area available for the reaction. Previous studies of the Mg_3N_2 decomposition described the formation of chemisorbed NH_4^+ as not limited by solid-state diffusion[36] and reported specific rate constants of the Mg_3N_2 hydrolysis on the same order as those reported here, which supports our interpretation.

NH_3 formation without solid-state diffusion control for Mg_3N_2 or Ca_3N_2 respectively is supported in addition by a correlation between the specific rate constant and the specific volumes of nitrides and the solid reaction products (Fig.5). This can be rationalized as particle breakup due to volume changes during the reaction (Fig.5). The reaction products were mixtures of the reacted metals, nitrides, and $Mg(OH)_2$/MgO, $Al(OH)_3/Al_2O_3$, $Ca(OH)_2$/CaO, Cr_2O_3, MnO/Mn_3O_4, ZnO, or MoO_3/MoO_2 (where the presence of the second solid in each pair increased with increasing temperature). Mg_3N_2 or Ca_3N_2 particles were decreased by about 89 or 57 % in diameter after hydrolysis, respectively. This can be explained with a specific volume increase from reactants to products. Hydrolysis of Zn_3N_2 led only to crevice formation (see additional online materials).

The activation energies of the NH_3 liberation (determined from Arrhenius plots of the specific rate constants given in Table 3) for Mg_3N_2 or Ca_3N_2 respectively are low, in the range of 9-14 kJ mol^{-1}. This is additional support for the assumed gas phase diffusion limitation since typical activation energies for solid-state diffusion limited processes are about 60 kJ mol^{-1} for the diffusion of Mn^{2+}, Mn^{3+}, or Mn^{4+} vacancies during the oxidation of Mn_3O_4[56] or about 135 kJ mol^{-1} (about 1.4 eV in average for a particle grain size ≥ 1 μm) for conduction in α-Al_2O_3[57]. The

approximate activation energies of 63, 92, 69, or 106 kJ mol^{-1} for the hydrolysis of Mn_4N, Cr_2N, Zn_3N_2 or AlN are within this range indicating solid-state diffusion limitation.

The observations and arguments above support that physical particle disintegration is likely the reason for the absence of solid-state diffusion limitations during the hydrolysis of the two tested highly ionic nitrides, Mg_3N_2 or Ca_3N_2. It will be shown in Section 4.4 that the solid-state diffusion limitations during the hydrolysis of the tested p- and d-block nitrides can be rationalized with the nitride ionicity.

4.3 Nitrogen mass balance

The nitrogen mass balance (Fig.4) neglects the relatively small amount of NH_3 detected in the vented gas phase (about 3.4-4.6 μmol NH_3 after 60 min via hydrolysis of Mg_3N_2 or Ca_3N_2 respectively). Figure 4 shows that all ionic nitrides are nearly completely oxidized after 60 min under steam. At 500°C 27-70 mol% of the removed N^{3-} is recovered as NH_3. All other nitrides except Mn_4N liberated less than 50 mol% of the lattice nitrogen with up to 17 mol% recovered as NH_3, except 41 ± 3 mol% NH_3 from 0.80 ± 0.01 mol% nitrogen liberated by AlN at 300°C or 60 ± 5 mol% NH_3 from 23 ± 2 mol% nitrogen liberated by Mo_2N at 500°C. Formation of N_2H_4 from Mn_4N was suspected[19] but back titration of the liquid absorbent did not confirm this (data not shown). The large amount of lattice nitrogen liberated from Mn_4N either does not form NH_3 effectively or NH_3 is formed but not removed quickly enough from the material surface due to Lewis or Brønsted acid-base interactions between manganese oxides, NH_3, H_2O and the related ionic species.

In summary, the efficient conversion of up to 70 mol% nitrogen liberated from ionic nitrides to NH_3 is matched in the reported experiments only by about 60 mol% NH_3 from the nitrogen of Mo_2N. The low yield of NH_3 from manganese nitride will be assessed elsewhere.

4.4 Nitride ionicity controlling the solid-state diffusion

Nitride hydrolysis yielding NH_3 is favored by a decrease in free energy (Fig.1B), impaired at elevated temperatures only by thermal decomposition of the nitrides or NH_3 to products and N_2. The reaction characteristics reported here are non-equilibrium. Ionic materials such as Mg_3N_2 yield NH_3 quickly. Less ionic nitrides such as Cr_2N liberate NH_3 slowly and only at elevated temperatures.

Attempting a relative comparison of the nitride hydrolysis data (Table 3), ionicity, i_N, here defined as the partial nitrogen charge[43-53] (Table 2) relative to a theoretical -3 oxidation state of the lattice nitrogen, $i_N = q_N/(-3)$, can be correlated with the specific rate constants k_s (Fig.6). This shows a promotion of the reaction kinetics by the partial electric charge of the lattice nitrogen, leveling off at about 35% ionicity (arrow, Fig.6). As reported for the diffusion of nitrogen or carbon in other solid-state processes[58], the effective diffusion coefficient appears dependent on the activity of the lattice nitrogen.

Limiting the focus on the p- and d-block nitrides (see Section 4.1), the effective chemical diffusion coefficient, D in $m^2\ s^{-1}$, is given with[54]:

$$(8) \qquad D = \frac{ad}{24c}\frac{\rho_{nitride} k_s d_p^2}{\rho_{steam}} \approx 8.54\times10^{-23}\exp\left(1.24\times10^{2}\times i_N\right)$$

where a, c, and d are stoichiometric coefficients (Eq.3) and $\rho_{nitride}$ and ρ_{steam} are the molar densities of the solid and gaseous reactants at 500°C in mol m^{-3} respectively. Figure 7 shows a plot of the diffusion coefficient versus the nominal radius of a single metal ion[6] (Fig.7A) or the nitride ionicity respectively (Fig.7B). The apparent bulk diffusion coefficient does not correlate with the nominal radius of a single metal ion but yields a nearly quantitative correlation ($R^2 > 0.97$) with the nitride ionicity.

For comparison, assuming a diffusion length equal to half the particle diameter yields the characteristic time[59] for a solid-state diffusion limited process, t_D, with approximately $d_p^2/(16D)$. The characteristic diffusion times (Fig.7B) for Cr_2N, AlN, or Mn_4N are about 206 days, 7.9 hrs, or 33.7 min respectively. This is by orders of magnitude longer than, e.g., the 0.1-2 ms range estimated for a solar thermochemical H_2 production cycle that had been assessed as not limited by the diffusion of oxygen vacancies in a ceria lattice[59]. The characteristic times for the NH_3 liberation from the nitrides with slightly higher ionicity, i.e., Mo_2N or Zn_3N_2 with 19.7 or 2.16 s respectively, are significantly shorter. This supports the inferred link between solid-state diffusion-controlled NH_3 formation and the ionicity, i.e., the partial charge of the nitrogen atom.

The diffusion coefficient is increasing with increasing ionicity suggesting that the size of hypothetical nitrogen ions with effective electric charges below three[50] is not determining the reaction kinetics. The nitride ionicity and its relation to the diffusion coefficient may be rather understood in terms of ambipolar diffusion that is the coupled migration of nitrogen ions (or vacancies respectively) and electrons under a nitrogen chemical potential gradient[59]. Increasing the nitride ionicity increases the volumetric concentration of reactive lattice nitrogen. This increases the diffusion coefficient (assuming generally a higher mobility of electrons in the conduction band[38] compared to the mobility of the nitrogen ions).

This dependency of the ammonia formation kinetics on of the nitride ionicity can be used to screen for optimized reactants. The ideal nitride for solar thermochemical NH_3 synthesis (see Section 2) has, on one hand, a reasonably stable metal nitrogen bond to enable the reduction of 0.1 MPa N_2 (opposed to, e.g., Zn_3N_2) without forming highly stable oxides (e.g., MgO or Al_2O_3)[28]. This narrows the focus on the transition metals. On the other hand, efficient and fast protonation of the lattice nitrogen to NH_3 requires nitride ionicities between those of Mo_2N and Zn_3N_2. The desired optimum may be found by screening the transition metal nitrides for their

partial electric nitrogen charge and/or by doping nitrides (e.g., those formed by Mo or Mn) with metals that donate additional electrons to the nitrogen without leading to formation of significantly more stable oxides during the hydrolysis (maybe small quantities of early transition metals such as Ti).

5. Conclusions

A rationale to design new reactants for solar thermochemical ammonia production from air and water based on ionicity has been developed. The correlation between the nitride ionicity and the effective solid-state diffusion coefficient that limits nitride hydrolysis (ammonia formation) suggests a reaction mechanism governed by the volumetric concentration of active nitrogen ions. Based on NH_3 liberation kinetics, the nitrogen mass balance and the minimum heat liberated during the hydrolysis step Mo_2N may be a promising major constituent of a reactant for the solar thermochemical NH_3 synthesis. Development of manganese-based reactants may benefit from efficient liberation of the lattice nitrogen but will require means to ensure an economic recovery of the nitrogen as NH_3.

Associated content

Supporting Information Available: An Ellingham diagram for the reduction of MgO, Al_2O_3, CaO, Cr_2O_3, Mn_2O_3, MnO, ZnO, MoO_2 and the oxidation of various reducing agents vs. temperature, the dependence of the free energy stored in the reaction cycle products (NH_3, H_2, or CO) on the stoichiometric composition of the nitride/oxide reactant, a detailed version of Fig.1A, a plot of the free energy of the N^{3-} oxidation reaction vs. the electronegativity of the metal constituent of the nitride, a complete version of Fig.4 providing kinetic NH_3 formation data and the nitrogen mass balance, and SEM micrographs of the Zn_3N_2 or Mo_2N hydrolysis respectively. This material is available free of charge via the Internet at http://pubs.acs.org.

Acknowledgments

Nam Nguyen, Kevin Turner, Elliott Meckley, and Kent E. Hampton are gratefully acknowledged for their technical assistance. Custom glass and quartz ware was manufactured by James R. Hodgson, Kansas State University. This material is based upon work supported by National Science Foundation Grant "From Crops to Commuting: Integrating the Social, Technological, and Agricultural Aspects of Renewable and Sustainable Biorefining (I-STAR)" NSF Award No.: DGE-0903701. Funding by the Center for Sustainable Energy, Kansas State University is gratefully acknowledged.

References

(1) Grätzel, M. *Chemistry Letters* **2005**, *34*, 8.

(2) Roeb, M.; Müller-Steinhagen, H. *Science* **2010**, *329*, 773.

(3) Smil, V. *Nature* **1999**, *400*, 415.

(4) Kirova-Yordanova, Z. *Energy* **2004**, *29*, 2373.

(5) Rafiqul, I.; Weber, C.; Lehmann, B.; Voss, A. *Energy* **2005**, *30*, 2487.

(6) Latscha, H. P.; Mutz, M. *Chemie der Elemente, Chemie-Basiswissen IV, ISBN 978-3-642-16914-4*; Springer: Heidelberg, 2011.

(7) Hellman, A.; Baerends, E. J.; Biczysko, M.; Bligaard, T.; Christensen, C. H.; Clary, D. C.; Dahl, S.; van Harrevelt, R.; Honkala, K.; Jonsson, H.; Kroes, G. J.; Luppi, M.; Manthe, U.; Nørskov, J. K.; Olsen, R. A.; Rossmeisl, J.; Skúlason, E.; Tautermann, C. S.; Varandas, A. J. C.; Vincent, J. K. *Journal of Physical Chemistry B* **2006**, *110*, 17719.

(8) Christensen, C. H.; Johannessen, T.; Sørensen, R. Z.; Nørskov, J. K. *Catalysis Today* **2006**, *111*, 140.

(9) Churchard, A. J.; Banach, E.; Borgschulte, A.; Caputo, R.; Chen, J.-C.; Clary, D. C.; Fijalkowski, K. J.; Geerlings, H.; Genova, R. V.; Grochala, W.; Jaroń, T.; Juanes-Marcos, J. C.; Kasemo, B.; Kroes, G.-J.; Ljubić, I.; Naujoks, N.; Nørskov, J. K.; Olsen, R. A.; Pendolino, F.; Remhof, A.; Románszki, L.; Tekin, A.; Vegge, T.; Zäch, M.; Züttel, A. *Physical Chemistry Chemical Physics* **2011**, *13*, 16955.

(10) Reiter, A. J.; Kong, S.-C. *Energy & Fuels* **2008**, *22*, 2963.

(11) Reiter, A. J.; Kong, S. C. *Fuel* **2011**, *90*, 87.

(12) Skúlason, E.; Bligaard, T.; Gudmundsdóttir, S.; Studt, F.; Rossmeisl, J.; Abild-Pedersen, F.; Vegge, T.; Jónsson, H.; Nørskov, J. K. *Physical Chemistry Chemical Physics* **2012**, *14*, 1235.

(13) Valov, I.; Luerssen, B.; Mutoro, E.; Gregoratti, L.; De Souza, R. A.; Bredow, T.; Günther, S.; Barinov, A.; Dudin, P.; Martin, M.; Janek, J. *Physical Chemistry Chemical Physics* **2011**, *13*, 3394.

(14) Lee, D.-K.; Fischer, C. C.; Valov, I.; Reinacher, J.; Stork, A.; Lerch, M.; Janek, J. *Physical Chemistry Chemical Physics* **2011**, *13*, 1239.

(15) Amar, I. A.; Lan, R.; Petit, C. T. G.; Tao, S. *Journal of Solid State Electrochemistry* **2011**, *15*, 1845.

(16) Marnellos, G.; Stoukides, M. *Science* **1998**, *282*, 98.

(17) Knobloch, D. J.; Lobkovsky, E.; Chirik, P. J. *Nature Chemistry* **2010**, *2*, 30.

(18) Fryzuk, M. D. *Accounts of Chemical Research* **2009**, *42*, 127.

(19) Gilbertson, J. D.; Szymczak, N. K.; Tyler, D. R. *Journal of the American Chemical Society* **2005**, *127*, 10184.

(20) Rodriguez, M. M.; Bill, E.; Brennessel, W. W.; Holland, P. L. *Science* **2011**, *334*, 780.

(21) Scheffe, J. R.; Li, J. H.; Weimer, A. W. *International Journal of Hydrogen Energy* **2010**, *35*, 3333.

(22) Chueh, W. C.; Falter, C.; Abbott, M.; Scipio, D.; Furler, P.; Haile, S. M.; Steinfeld, A. *Science* **2010**, *330*, 1797.

(23) Stamatiou, A.; Loutzenhiser, P. G.; Steinfeld, A. *Energy & Fuels* **2010**, *24*, 2716.

(24) Miller, J. E.; Allendorf, M. D.; Diver, R. B.; Evans, L. R.; Siegel, N. P.; Stuecker, J. N. *Journal of Materials Science* **2008**, *43*, 4714.

(25) Licht, S.; Wang, B.; Wu, H. *Journal of Physical Chemistry C* **2011**, *115*, 11803.

(26) Gálvez, M. E.; Halmann, M.; Steinfeld, A. *Industrial & Engineering Chemistry Research* **2007**, *46*, 2042.

(27) Michalsky, R.; Pfromm, P. H. *Solar Energy* **2011**, *85*, 2642.

(28) Michalsky, R.; Pfromm, P. H. *AIChE Journal,* DOI 10.1002/aic.13717 (**in press)**.

(29) Michalsky, R.; Parman, B. J.; Amanor-Boadu, V.; Pfromm, P. H. *Energy* **2012**, *42*, 251.

(30) Barin, I.; Knacke, O. *Thermochemical properties of inorganic substances*; Springer-Verlag: Berlin Heidelberg New York, 1973.

(31) Warner, J. W.; Berry, R. S. *Journal of Physical Chemistry* **1987**, *91*, 2216.

(32) Shaffer, P. T. B. *Plenum Press Handbooks of High-Temperature materials, No.1 Materials Index*; Plenum Press: New York, 1964.

(33) Baba, H.; Katada, Y. *Corrosion Science* **2006**, *48*, 2510.

(34) Gálvez, M. E.; Frei, A.; Halmann, M.; Steinfeld, A. *Industrial & Engineering Chemistry Research* **2007**, *46*, 2047.

(35) Fukumoto, S.; Hookabe, T.; Tsubakino, H. *Journal of Materials Science* **2000**, *35*, 2743.

(36) Heyns, A. M.; Prinsloo, L. C.; Range, K. J.; Stassen, M. *Journal of Solid State Chemistry* **1998**, *137*, 33.

(37) Weidman, M. C.; Esposito, D. V.; Hsu, Y. C.; Chen, J. G. *Journal of Power Sources* **2012**, *202*, 11.

(38) Gregory, D. H. *Journal of the Chemical Society-Dalton Transactions* **1999**, 259.

(39) Mowbray, D. J.; Martínez, J. I.; Calle-Vallejo, F.; Rossmeisl, J.; Thygesen, K. S.; Jacobsen, K. W.; Nørskov, J. K. *Journal of Physical Chemistry C* **2011**, *115*, 2244.

(40) Rossmeisl, J.; Nørskov, J. K.; Taylor, C. D.; Janik, M. J.; Neurock, M. *Journal of Physical Chemistry B* **2006**, *110*, 21833.

(41) Jacobsen, C. J. H.; Dahl, S.; Clausen, B. S.; Bahn, S.; Logadottir, A.; Nørskov, J. K. *Journal of the American Chemical Society* **2001**, *123*, 8404.

(42) Cairns, A. G.; Gallagher, J. G.; Hargreaves, J. S. J.; McKay, D.; Rico, J. L.; Wilson, K. *Journal of Solid State Chemistry* **2010**, *183*, 613.

(43) Chen, Y. H.; Kang, L.; Zhang, C. R.; Luo, Y. C.; Wu, Z. M.; Zhang, M. L. *Chinese Journal of Inorganic Chemistry* **2008**, *24*, 1029.

(44) Sharma, H.; Garg, I.; Dharamvir, K.; Jindal, V. K. *Journal of Computational and Theoretical Nanoscience* **2010**, *7*, 2297.

(45) Bai, Q.; Song, B.; Hou, J.; He, P. *Physics Letters A* **2008**, *372*, 4545.

(46) Chen, Y.-H.; Kang, L.; Zhang, C.-R.; Luo, Y.-C.; Yuan, L.-H.; Li, Y.-L. *Acta Physica Sinica* **2008**, *57*, 6265.

(47) Chaudhari, A.; Lee, S.-L. *International Journal of Quantum Chemistry* **2007**, *107*, 212.

(48) Blomberg, M. R. A.; Siegbahn, P. E. M. *Theoretica Chimica Acta* **1992**, *81*, 365.

(49) Mola, E. E.; Coronel, E.; Joly, Y.; Vicente, J. L. *Langmuir* **1988**, *4*, 917.

(50) Nagakura, S.; Ōtsuka, N. *Journal of the Physical Society of Japan* **1975**, *39*, 1047.

(51) Li, Z.; Wang, P.; Chen, H.; Cheng, X. *Physica B-Condensed Matter* **2011**, *406*, 1182.

(52) Chen, H.; Lei, X. L.; Liu, L. R.; Liu, Z. F.; Zhu, H. J. *Chinese Physics B* **2010**, *19*.

(53) Qi, J.; Jiang, L. H.; Jiang, Q. A.; Wang, S. L.; Sun, G. Q. *Journal of Physical Chemistry C* **2010**, *114*, 18159.

(54) Levenspiel, O. *Chemical reaction engineering, Third Edition, Chapter 25 Fluid-particle reactions: Kinetics*; John Wiley & Sons: New York, 1999.

(55) Ettmayer, P. *Monatshefte für Chemie* **1970**, *101*, 127.

(56) Gillot, B.; El Guendouzi, M.; Laarj, M. *Materials Chemistry and Physics* **2001**, *70*, 54.

(57) Öijerholm, J. *Division of Corrosion Science, Department of Chemistry, School of Chemical Science and Engineering, Royal Institute of Technology, Stockholm, 2007*.

(58) Christiansen, T. L.; Somers, M. A. J. *International Journal of Materials Research* **2008**, *99*, 999.

(59) Chueh, W. C.; Haile, S. M. *Philosophical Transactions of the Royal Society a-Mathematical Physical and Engineering Sciences* **2010**, *368*, 3269.

Tables

Table 1. Characterization of the metal nitride powder beds

nitride	Mg_3N_2	w-AlN	α-Ca_3N_2 (Ca_2N)	Cr_2N (CrN)	Mn_4N ($Mn_6N_{2.58}$)	Zn_3N_2	β-Mo_2N
space group	*Ia*-3	*P*6$_3$*mc*	*Ia*-3 (*R*-3*m*)	*P*-31*m* (*Fm*-3*m*)	*Pm*-3*m* (*P*6$_3$22)	*Ia*-3	*I*4$_1$/*amd*
$x_{nitride}$ [a] (wt%)	100 ± 1	100 ± 1	86 ± 5 (14 ± 5)	85 ± 1 (10.1 ± 0.3)	70 ± 5 (28 ± 3)	100 ± 1	24.9 ± 0.4
$\langle d_{nitride} \rangle$ [b] (µm)	27 ± 11	16 ± 6	105 ± 25	43 ± 14	46 ± 19	21 ± 7	13 ± 6
A_{BET} [c] ($m^2\ g^{-1}$)	8.8 ± 0.3	4.9 ± 0.1	0.67 ± 0.01	0.40 ± 0.01	0.27 ± 0.01	3.75 ± 0.03	0.43 ± 0.01
A_{bed} [d] (cm^2)	42	42	42	33	33	42	33
Φ [e] ($m^3\ m^{-3}$)	0.68	0.69	0.55	0.55	0.65	0.73	0.73

a, nitride weight fraction; *b*, average particle diameter; *c*, BET surface area; *d*, powder bed surface ± 5.24 % (via error propagation), powder bed thickness generally < 1 mm; *e*, void space fraction ± 5.15 % (via error propagation)

Table 2. Partial nitrogen charge of binary metal nitrides

nitride	q_N [a]	methods
Mg_3N_2	-2.06 ± 0.19	MPA [43]
w-AlN	-0.36 ± 0.05	MPA [44,45]
α-Ca_3N_2 (Ca_2N)	-1.91 ± 0.29	MPA for Ca_3N_2 [46]
Cr_2N (CrN)	-0.30 ± 0.03	MPA for CrN [47],CASSCF for CrN [48], MNDO [b] for Cr_2N [49]
Mn_4N ($Mn_6N_{2.58}$)	-0.47 ± 0.18	electron diffraction for Mn_4N [50], MPA for MnN [47]
Zn_3N_2	-0.64	MPA [51]
β-Mo_2N	-0.53 ± 0.10	MPA for $Mo_{2n}N_n$ clusters with n ≥ 4 [52], MPA [53]

a, The partial nitrogen charge q_N (in units of the elementary charge e) is given as arithmetic average with one standard deviation of up to 12 literature values; *b*, neglecting a relative high value for CrN; MPA, Mulliken population analysis; CASSCF, complete-active-space self-consistent-field; MNDO, modified neglect of diatomic overlap.

Table 3. Kinetic data and modeling [a]

metal as nitride	T_{hyd} (°C)	r_0 (mol_{NH3} mol_{metal}^{-1} s^{-1})	model	k (s^{-1})	R^2 >	Δt_{fit} (min)
ionic nitrides						
Mg	200	$1.0 \pm 0.2 \times 10^{-4}$	g	6.2×10^{-4}	0.80	10
	300	$2.3 \pm 0.4 \times 10^{-5}$	g	9.7×10^{-5}	0.99	60
	500	$1.1 \pm 0.2 \times 10^{-3}$	g [b]	1.2×10^{-3}	0.90	10
Ca	200	$1.4 \pm 0.2 \times 10^{-5}$	g [b]	7.7×10^{-5}	0.99	60
	300	$4.3 \pm 0.6 \times 10^{-6}$	g [b]	4.4×10^{-5}	0.90	60
	500	$1.6 \pm 0.2 \times 10^{-5}$	g [b]	2.9×10^{-4}	0.75	60
Zn	300	$8 \pm 1 \times 10^{-7}$	s	3.3×10^{-10}	0.87	10
	500	$3.3 \pm 0.6 \times 10^{-4}$	g	8.9×10^{-4}	0.91	10
	1000	$2.9 \pm 0.4 \times 10^{-4}$	s	2.8×10^{-5}	0.72	5
covalent nitrides						
Al	300	$9 \pm 2 \times 10^{-8}$	s	6.3×10^{-13}	0.96	10
	500	$8 \pm 1 \times 10^{-6}$	s	6.9×10^{-9}	0.92	60
	1000	$4.9 \pm 0.8 \times 10^{-5}$	s	1.4×10^{-7}	0.88	60
interstitial and intermediate nitrides						
Cr	500	$1.5 \pm 0.3 \times 10^{-7}$	s	7.6×10^{-12}	0.80	30
	600	$1.0 \pm 0.2 \times 10^{-7}$	s	3.3×10^{-12}	0.95	10
	1000	$1.8 \pm 0.3 \times 10^{-6}$	s	1.2×10^{-9}	0.99	30
Mn	300	$8 \pm 1 \times 10^{-8}$	r [b]	8.2×10^{-8}	0.98	30
	500	$9.7 \pm 0.9 \times 10^{-6}$	s	6.9×10^{-8}	0.93	60
	1000	$5.3 \pm 0.7 \times 10^{-6}$	s	3.6×10^{-8}	0.96	30
Mo	500	$3.2 \pm 0.3 \times 10^{-5}$	s	6.4×10^{-6}	0.82	30
	600	$4.9 \pm 0.7 \times 10^{-6}$	s	1.5×10^{-7}	0.88	30
	1000	$7 \pm 1 \times 10^{-6}$	s	4.0×10^{-7}	0.85	30

a, Applying shrinking core models (controlled by: s, diffusion through the solid reaction product; r, reaction; g, diffusion through the gas film) in the time range Δt_{fit}. *b*, r or g respectively show an only slightly (< 0.05) lower R^2 value.

Schemes and Charts

Scheme 1. Two-step reactive NH_3 synthesis from N_2, H_2O and solar heat

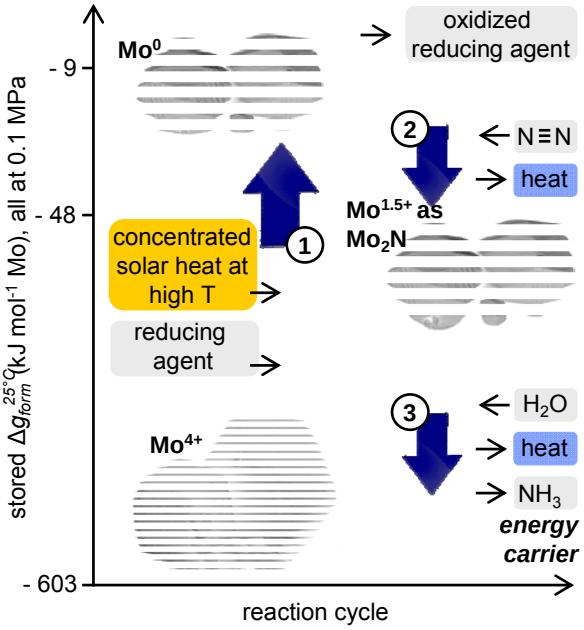

The endothermic reduction (1) of an oxidized material (e.g., Mo^{4+}) and the exothermic reduction of N_2 (2) may be conducted in one step. This generates nominally N^{3-} that can be protonated with H_2O (3).

Chart 1. Schematic protonation of reduced nitrogen

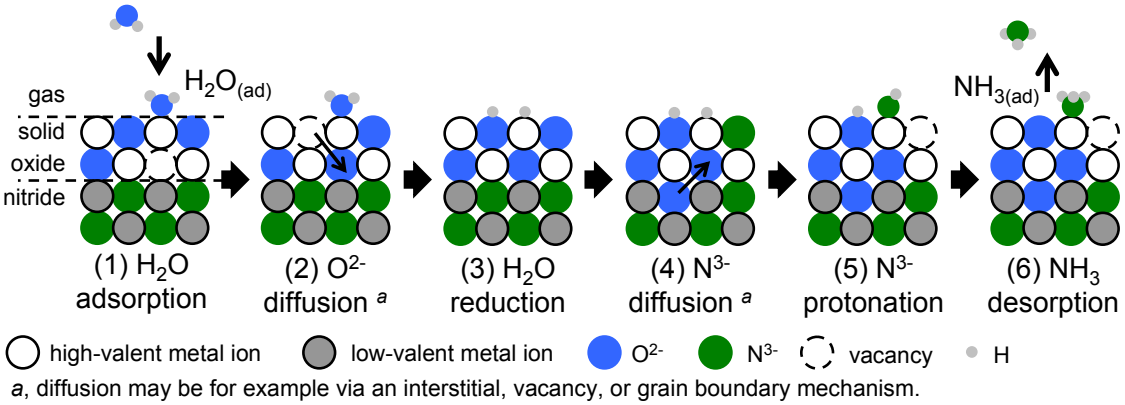

a, diffusion may be for example via an interstitial, vacancy, or grain boundary mechanism.

Figure captions

Figure 1: Rationale for the choice of metals: (A) Enthalpy[30] mapping of the exothermic heat liberated during the N^{3-} oxidation ($\Delta h_{N3-\ ox.}$, Eq.3) versus N_2 reduction ($\Delta h_{N2\ red.}$, Eq.2), both relative to the energy supplied during the solar-thermal metal oxide reduction step (Eq.1). Empty circles mark materials that do not fix 0.1 MPa N_2, do not liberate NH_3 effectively, or are radioactive (see online materials). (B) Correlation of $\Delta h_{N3-\ ox.}$ with the free energy[30] of the reaction ($\Delta g_{N3-\ ox.}$). All computations are at 25°C and 0.1 MPa.

Figure 2: Correlation between the bulk heat of formation[30] for transition metal nitrides, g_f, in kJ mol^{-1} lattice nitrogen versus the number of d electrons, N_d. A nearly quantitative linear correlation (solid line) is obtained when excluding elements with nominally only one d electron or with a completely occupied $3d^{10}$ orbital (empty circles, dashed line).

Figure 3: Experimental setups (*a*, N_2 gas; *b*, H_2 gas, *c*, flow meter; *d*, gas mixing; *e*, tubular flow-through furnace; *f*, metal powder in quartz boat; *g*, heating plate; *h*, liquid level control; *i*, liquid H_2O; *j*, metal nitride powder in quartz boat; *k*, magnetic stirrer; *l*, 10 mM HCl chilled with ice-cold H_2O; *m*, NH_3 gas detection tube).

Figure 4: Representative results (see online materials) for steam hydrolysis of metal nitride powders illustrating the kinetic fitting with maximized R^2 (see Table 3): (A) solid-state diffusion-governed NH_3 formation from Al (circle), Cr (diamond), Mn (triangle), and Mo (square) nitrides and (B) the supply of H_2O from the gas phase controlling NH_3 formation from Mg (circle), Ca (diamond) and Zn (triangle, at 500°C, see Table 3) nitrides. Error bars are via error propagation.

Figure 5: The specific rate constant k (maximum R^2, Table 3) versus the specific volume change (Δv_{hyd}) when oxidizing the nitrides at 300°C (ρ_i is the density in mol m^{-3} of substance i). Error bars are three standard deviations; R^2 for the fit (line) is > 0.91. SEM images are representative nitrides of (*a*) or (*b*) Mn, and (*c*) or (*d*) Ca before or after the hydrolysis respectively.

Figure 6: The specific rate constant k_s at 300°C (circles, solid line fit with $R^2 > 0.99$) or 500°C (diamonds, fit excluding Zn^{2+} with $R^2 > 0.76$) versus nitride ionicity (arrow see Section 4.4). Metal cations indicated mark the oxides/hydroxides detected after hydrolysis. Error propagation using three standard deviations yields in average ca. ± 2.22% (300°C) or ± 3.23% (500°C).

Figure 7: The diffusion coefficient D for steam hydrolysis at 500°C plotted against (A) the nominal radius of a single metal ion with $R^2 > 0.28$ or (B) the nitride ionicity with $R^2 > 0.97$. The inlet shows the characteristic time for the diffusion process with $R^2 > 0.96$. R^2 computations are based on the data set without Mg^{2+} and Ca^{2+}. Error bars on the ordinate are via error propagation.

Figures

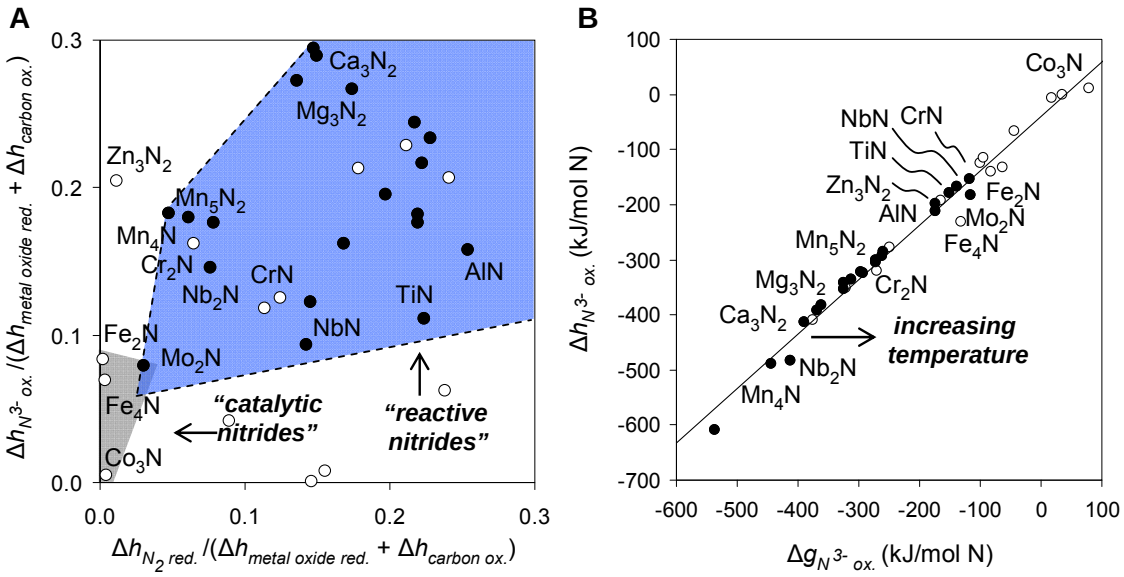

Figure 1: Rationale for the choice of metals: (A) Enthalpy[30] mapping of the exothermic heat liberated during the N^{3-} oxidation ($\Delta h_{N3-\ ox.}$, Eq.3) versus N_2 reduction ($\Delta h_{N2\ red.}$, Eq.2), both relative to the energy supplied during the solar-thermal metal oxide reduction step (Eq.1). Empty circles mark materials that do not fix 0.1 MPa N_2, do not liberate NH_3 effectively, or are radioactive (see online materials). (B) Correlation of $\Delta h_{N3-\ ox.}$ with the free energy[30] of the reaction ($\Delta g_{N3-\ ox.}$). All computations are at 25°C and 0.1 MPa.

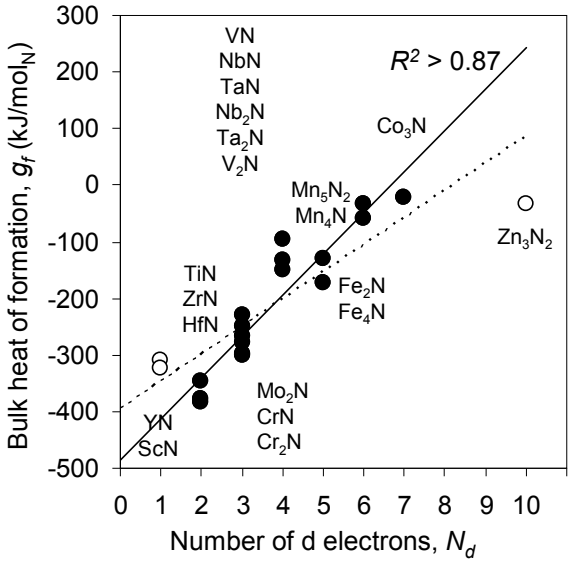

Figure 2: Correlation between the bulk heat of formation[30] for transition metal nitrides, g_f, in kJ mol^{-1} lattice nitrogen versus the number of d electrons, N_d. A nearly quantitative linear correlation (solid line) is obtained when excluding elements with nominally only one d electron or with a completely occupied $3d^{10}$ orbital (empty circles, dashed line).

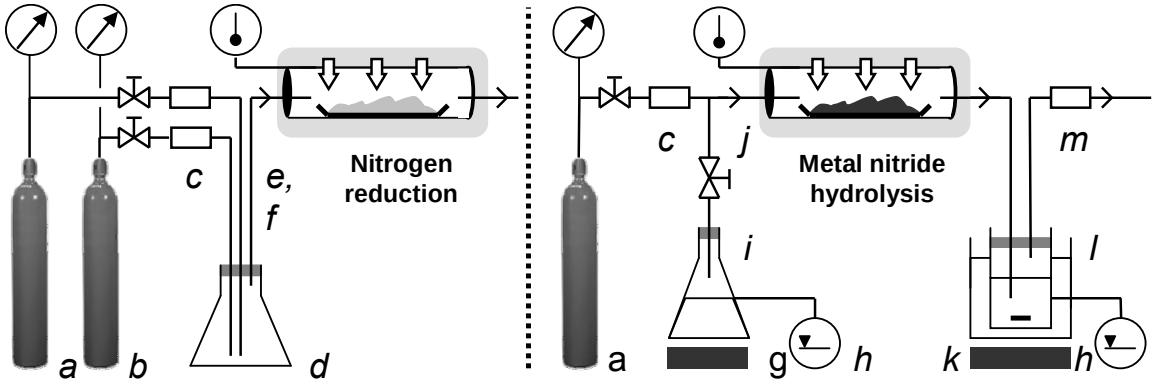

Figure 3: Experimental setups (*a*, N_2 gas; *b*, H_2 gas, *c*, flow meter; *d*, gas mixing; *e*, tubular flow-through furnace; *f*, metal powder in quartz boat; *g*, heating plate; *h*, liquid level control; *i*, liquid H_2O; *j*, metal nitride powder in quartz boat; *k*, magnetic stirrer; *l*, 10 mM HCl chilled with ice-cold H_2O; *m*, NH_3 gas detection tube).

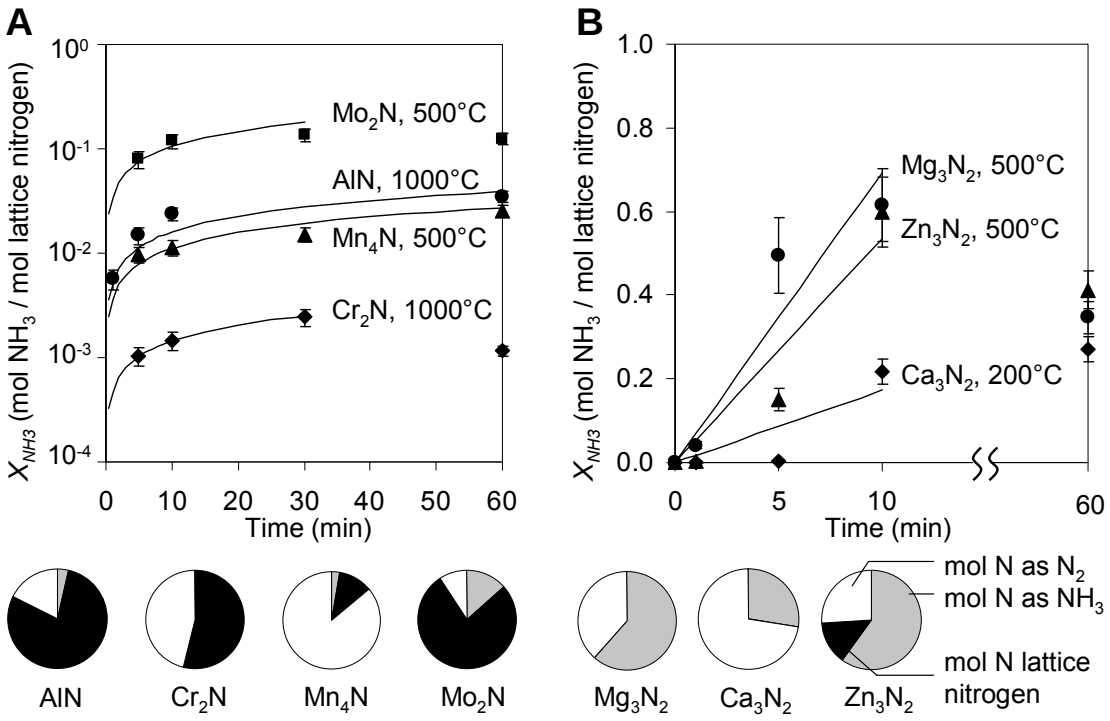

Figure 4: Representative results (see online materials) for steam hydrolysis of metal nitride powders illustrating the kinetic fitting with maximized R^2 (see Table 3): (A) solid-state diffusion-governed NH_3 formation from Al (circle), Cr (diamond), Mn (triangle), and Mo (square) nitrides and (B) the supply of H_2O from the gas phase controlling NH_3 formation from Mg (circle), Ca (diamond) and Zn (triangle, at 500°C, see Table 3) nitrides. Error bars are via error propagation.

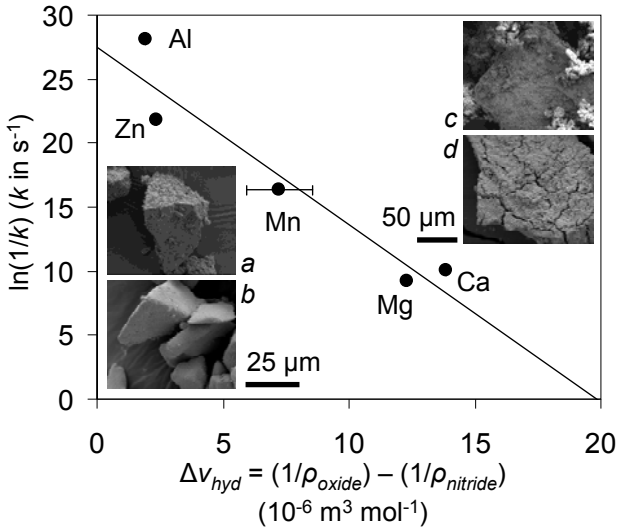

Figure 5: The specific rate constant k (maximum R^2, Table 3) versus the specific volume change (Δv_{hyd}) when oxidizing the nitrides at 300°C (ρ_i is the density in mol m^{-3} of substance i). Error bars are three standard deviations; R^2 for the fit (line) is > 0.91. SEM images are representative nitrides of (*a*) or (*b*) Mn, and (*c*) or (*d*) Ca before or after the hydrolysis respectively.

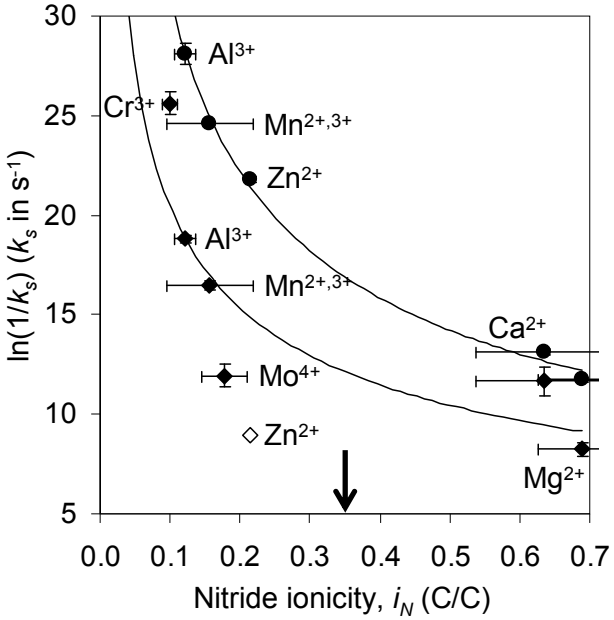

Figure 6: The specific rate constant k_s at 300°C (circles, solid line fit with $R^2 > 0.99$) or 500°C (diamonds, fit excluding Zn^{2+} with $R^2 > 0.76$) versus nitride ionicity (arrow see Section 4.4). Metal cations indicated mark the oxides/hydroxides detected after hydrolysis. Error propagation using three standard deviations yields in average ca. ± 2.22% (300°C) or ± 3.23% (500°C).

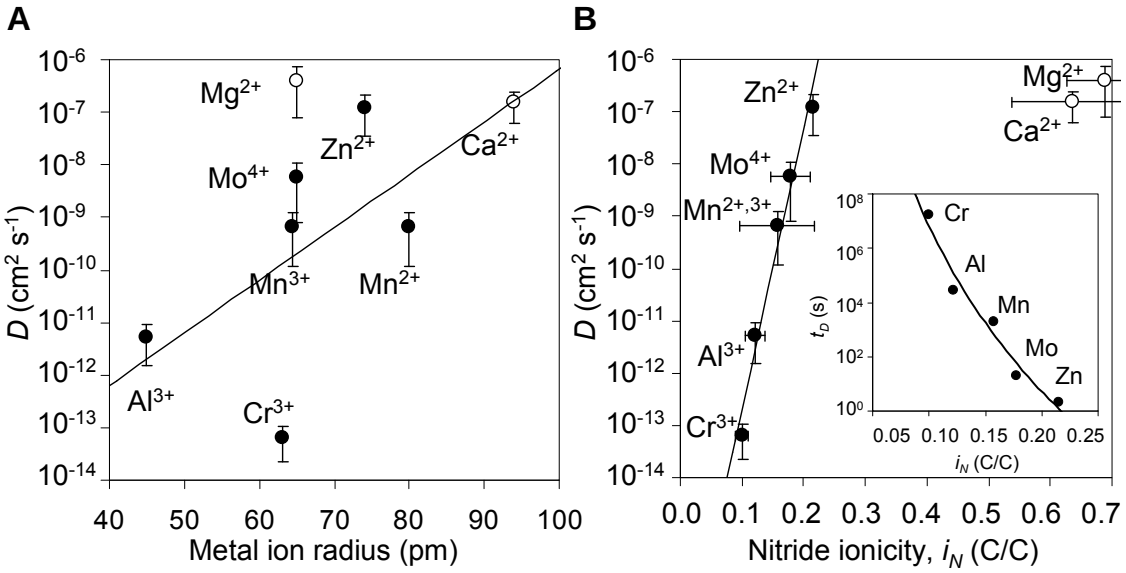

Figure 7: The diffusion coefficient D for steam hydrolysis at 500°C plotted against (A) the nominal radius of a single metal ion with $R^2 > 0.28$ or (B) the nitride ionicity with $R^2 > 0.97$. The inlet shows the characteristic time for the diffusion process with $R^2 > 0.96$. R^2 computations are based on the data set without Mg^{2+} and Ca^{2+}. Error bars on the ordinate are via error propagation.

Online Table of Content Image